# HiPSC encapsulation geometry impacts 3D developing human engineered cardiac tissue functionality

## Author Names:

Morgan E. Ellis¹, meb0089@auburn.edu
Bryana N. Harris¹, bnh0018@tauburn.edu
Mohammadjafar Hashemi¹, mzh0111@auburn.edu
B. Justin Harvell¹, bjh0076@auburn.edu
Michaela Z. Bush¹, mzb0108@auburn.edu
Emma E. Hicks¹, eeh0019@auburn.edu
Ferdous B. Finklea¹, fbt0001@auburn.edu
Eric M. Wang¹, ezw0044@auburn.edu
Ravikiran Nataraj¹, rzn0039@auburn.edu
Nathan P. Young¹, npy0001@auburn.edu
Irene C. Turnbull², irene.turnbull@mssm.edu
Elizabeth A. Lipke¹\*, eal0003@auburn.edu

## Affiliation:

Keywords: cardiac differentiation, human induced pluripotent stem cells, tissue geometry, engineered heart tissue

<sup>&</sup>lt;sup>1</sup> Department of Chemical Engineering, 212 Ross Hall, Auburn University, Auburn, AL 36849, 334-844-2033

<sup>&</sup>lt;sup>2</sup> Cardiovascular Research Institute, Icahn School of Medicine at Mount Sinai, 1470 Madison Ave, New York, NY 10029, 212-241-6500

<sup>\*</sup> Corresponding author: <a href="mailto:elipke@auburn.edu">elipke@auburn.edu</a>

## Abstract

Cardiac tissue engineering has been working to alleviate the immense burden of cardiovascular disease for several decades. To improve cardiac tissue homogeneity and cardiomyocyte (CM) maturation, here we investigated altering initial encapsulation geometry in a 3D direct cardiac differentiation platform. Traditional engineered cardiac tissue production utilizes predifferentiated CMs to produce 3D cardiac tissue and often involves various cell selection and exogenous stimulation methods to promote CM maturation. Starting tissue formation directly with human induced pluripotent stem cells (hiPSCs), rather than pre-differentiated CMs, simplifies the engineered cardiac tissue formation process making it more applicable for widespread implementation and scale-up. Here, hiPSCs were encapsulated in PEG-fibrinogen in three tissue geometries (disc-shaped microislands, squares, and rectangles) and subjected to established cardiac differentiation protocols. Resulting 3D engineered cardiac tissues (3D-ECTs) from each geometry displayed similar CM populations (~ 65%) and gene expression over time. Notably, rectangular tissues displayed less tissue heterogeneity and suggested more advanced features of maturing CMs including myofibrillar alignment and Z-line formation. Additionally, rectangular tissue showed significantly higher anisotropic contractile properties compared to square and microisland tissues (MI  $0.28 \pm 0.03$ , SQ  $0.35 \pm 0.05$ , RT  $0.79 \pm 0.04$ ). This study demonstrates a straightforward method for simplifying and improving 3D-ECT production without the use of exogenous mechanical or electrical pacing and has the potential to be utilized in bioprinting and drug testing applications.

# **Impact Statement:**

Current methods for improving cardiac maturation post-differentiation remain tedious and complex. Here, we examined the impact of initial encapsulation geometry on improvement of 3D engineered cardiac tissue (3D-ECT) production and post-differentiation maturation for three tissue geometries including disc-shaped microislands, squares, and rectangles. Notably, rectangular 3D-ECTs displayed less tissue heterogeneity and more advanced features of maturing cardiomyocytes including myofibrillar alignment, Z-line formation, and anisotropic contractile properties compared to microisland and square tissues. This study demonstrates an initial hiPSC-encapsulated rectangular tissue geometry can improve cardiac maturation, rather than implementing cell selection or tedious post-differentiation manipulation including exogenous mechanical and/or electrical pacing.

## Introduction

Heart disease is the leading cause of death worldwide in both men and women of nearly all ethnicities(1). With limited regenerative capacity, diseased cardiac tissue is not able to fulfill its electrical and mechanical roles, including electrical signal propagation and blood circulation, often leading to arrhythmias and sudden cardiac death. Heart transplants remain the standard of care for treating heart failure, but as a result of the highly limited supply of organs for transplant, this costly and invasive option is not always available (2). Cardiac tissue engineering provides the potential to create functional replacement tissues for use in cardiac regenerative medicine and as an *in vitro* platform for testing new therapeutics.

With the discovery of human induced pluripotent stem cells (hiPSCs) in 2007 (3), employing hiPSC-derived cardiomyocytes (hiPSC-CMs) has become customary in the field of cardiac tissue engineering. HiPSCs are differentiated down the cardiac lineage using a series of small molecules and growth factors, often in the form of embryoid bodies (4, 5) or monolayers (6, 7). Extensive research is being conducted using hiPSC-CMs to recapitulate the native tissue functionality, but there are major challenges in producing cells that mature to the adult CM phenotype, in particular with respect to cell morphology and alignment, electrophysiological function, calcium handling, and gap junction distribution (8, 9).

One of the key components of cardiac maturation *in vivo* is the alignment of CMs to form highly aligned myofibers, which are important for contraction (10) and electrophysiological function (11). In the native myocardium, the CMs orient themselves longitudinally to allow for electric coupling through intercalated discs at the ends of the rod-shaped cells, where most of the gap junctions reside, resulting in anisotropic action potential propagation (12). The organization and distribution of gap junctions in neighboring cells determines the current resistance, and therefore electrical

function of the tissue (13). *In vivo*, anisotropic action potential results in faster propagation in the longitudinal direction than in the transverse direction (14). This orientation allows for the individual cardiomyocytes to function together as a single contractile tissue for proper cardiac function. *In vitro*, engineered cardiac tissues often contain fetal-like CMs with randomly dispersed gap junctions, resulting in isotropic action potential propagation (8). Improving *in vitro* CM morphology and alignment, thereby promoting CM maturation, is critical for applicability in therapeutic testing and disease modeling.

Several techniques have been employed to improve cell organization in vitro, including microand nano-patterning (15, 16). However, these experiments often required specialized equipment and are performed in 2D monolayers rather than 3D tissues. Additionally, many of these platforms require pre-differentiated CMs which prevents us from studying CM alignment throughout development. The platform employed here provides a simplified, less labor-intensive approach to producing 3D engineered cardiac tissue that does not require predifferentiated cardiomyocytes or specialized equipment for driving maturation. While other systems have to initiate tissue production and differentiation prior to implementing the maturation strategy, our method incorporates the maturation strategy into the initial tissue production step. We have previously shown the ability to encapsulate hiPSCs in poly (ethylene glycol) fibringen (PEG-fibringen) to form 3D human engineered cardiac tissues (3D-ECTs) in a "microisland" disc-shaped geometry. While this study was highly successful, resulting in 3D-ECTs that presented with T-tubules adjacent to Z-lines, a key component of functional maturation (17), contraction often propagated in a circular direction along the edges of the microisland, which is not typical of contracting human myocardium.

In this study, we investigated the promotion of cardiac tissue maturation on the macroscale by changing the initial hiPSC encapsulation geometry. To do this, we compared three different tissue geometries: a rectangular tissue with a 5:1 length to width ratio, a square tissue with a 1:1 length to width ratio, and our established microisland geometry. The square geometry was selected to mimic the microislands while providing a straight outer edge for alignment. The rectangular geometry was designed to simulate a linear representation of the dense tissue ring that we saw in previous studies. Here we show that the rectangular geometry resulted in less tissue heterogeneity and improved cardiac tissue maturation resulting in the tissues more closely mimicking the native myocardium. The knowledge gained in this study will impact future production of engineered cardiac tissue for studying disease mechanisms and cardiac developmental biology.

# Methods

All materials were purchased from Sigma-Aldrich unless otherwise stated.

# 3D-ECT formation

HiPSCs were dissociated using Versene for 4.5 minutes at 37 °C. HiPSCs were resuspended in mTeSR medium and centrifuged for 5 minutes at 200g. The supernatant was removed leaving a cell pellet which was resuspended in polymer precursor solution at a concentration of 60 million hiPSCs/ml of precursor solution using a wide orifice pipet. Eight microliters of cell suspension was pipetted into each tissue geometry mold on acrylated glass coverslips. The solution was crosslinked using visible light for 30 seconds. The PDMS mold was carefully removed, and the attached tissues were placed in a 6-well plate with 3 mL of mTeSR medium supplemented with 10

μM RI (day -3). On the following two days (day -2, day -1) the spent media was replaced with 3 mL of fresh mTeSR media. On day 0, cardiac differentiation was initiated using established protocols (6) where 12 μM CHIR99021 was added to RPMI B27 minus insulin (Thermo Fisher Scientific). Exactly 24 hours later (day 1), the media was replaced with fresh RPMI B27 minus insulin. Exactly 48 hours later (day 3), half of the spent media was combined with an equal amount of fresh RPMI B27 minus insulin supplemented with 5 μM IWP2. Exactly 48 hours later (day 5), spent media was replaced with fresh RPMI B27 minus insulin. On day 7 and every 3 days thereafter, 3D engineered cardiac tissues (3D-ECTs) were fed with RMPI B27.

All methods for glass acrylation, PDMS mold preparation, PEG-fibrinogen synthesis, hiPSC cultture and tissue characterization are listed in the Supplementary Methods.

## **Results**

HiPSCs were encapsulated in three tissue geometries prior to cardiac differentiation.

In this study, we demonstrate that initial encapsulation geometry of hiPSCs impacts the functionality of resulting 3D-ECTs. Building on prior work, molds were designed to ascertain whether a straight edge and shorter edge to middle distance would promote CM alignment and maturation. The microisland geometry served as the control, with an edge to middle distance of 2 mm and tissue thickness of 700-800 µm. The square geometry design incorporated straight edges while maintaining the 2 mm edge to middle distance. The rectangular geometry design aimed to mimic a straightened version of the outer ring that formed throughout the microisland differentiation, with an edge to middle distance of 0.75 to 1 mm at any given point along the length of the rectangle. Custom PDMS molds in microisland, square, and rectangular geometries were produced using 3D printed positive casts (Supplementary Figure 1) such that all geometries would

have the same initial tissue volume and thickness. HiPSCs were encapsulated at 60 million cells per mL in PEG-fibrinogen (Figure 1) in each geometry similar to previously established methods (17, 18) via free radical polymerization using the photoinitiator Eosin Y and visible light. On day -2 (24 h post encapsulation), hiPSC colonies appeared evenly distributed throughout in all tissue geometries (Figure 1).

HiPSCs remained viable throughout encapsulation and differentiation.

Cell viability was monitored throughout differentiation in regions on the edge and middle of each tissue. On day -2 (24 hours post encapsulation), viable cell density appeared uniform both within and between each tissue geometry (Figure 2a and Supplementary Figure 3). At the onset of differentiation on day 0, viable cell colonies both on the edge and in the middle increased in size for all tissue geometries as hiPSCs proliferated in the 3D PEG-fibrinogen microenvironment; PEG-fibrinogen can be degraded and remodeled by encapsulated cells (19). By day 7 of differentiation, viable cell density was similarly uniformly distributed around the edges of each tissue geometry; however, this uniform distribution of viable cells was not maintained in the middle regions of microisland and square tissues (Supplementary Figure 3). Rectangular tissues showed a more homogenous regional cell viability throughout differentiation. Tissue area for each geometry increased comparably (MI 31.0  $\pm$  3.3%, SQ 28.4  $\pm$  4.5%, RT 27.5  $\pm$  2.9%) throughout differentiation from day -2 to day 7 (Figure 2b).

Engineered cardiac tissue geometry does not impact cardiac differentiation.

On day 10 of differentiation, cell population was analyzed by dissociating 3D-ECTs and performing flow cytometry using a fixable viability dye and cardiac markers, cTnT and MF20. All

tissue geometries showed similar percentages of cTnT+ cells (cTnT: MI 59.5  $\pm$  10.1%, SQ 61.4  $\pm$  5.8%, RT 66.7 $\pm$  4.6%; MF20 MI 57.9  $\pm$  10.2%, SQ 61.7 $\pm$  6.1%, RT 67.0 $\pm$  5.3% ) (Figure 3a-d,f) as expected for this differentiation protocol without the use of cardiomyocyte selection (17, 18).

Cardiac maturation was also assessed via RT-qPCR using a variety of genes that influence electrophysiology, calcium handling, contractility, and extracellular matrix production. 3D-ECTs from each geometry showed temporally appropriate changes in gene expression (Figure 3 e, g, Supplementary Figure 4). No significant differences were observed between tissue geometries at each time point, which is somewhat expected; the outer rings of the microisland and edges of the square tissues, which is where the majority of the cells are located, develop and mature similarly to the rectangular tissues throughout differentiation. Cardiac gene MYH7 (β-myosin heavy chain, β-MHC) expression increased over time with a subsequent temporal decrease of MYH6 (α-myosin heavy chain,  $\alpha$ -MHC) expression, revealing a transition from fetal isoform  $\alpha$ -MHC to the adult isoform β-MHC (Supplementary Figure 4e, f). Additionally, MYL2 (ventricular myosin light chain 2, MLC2v) expression increased over culture time as expected based on previous studies (Supplementary Figure 4g) (17). All geometries showed increased expression of GJA5 (connexin 40, CX40) and COL3A1 (Collagen Type III Alpha 1 Chain) over time (Supplementary Figure 4d, k). Microisland and square geometries showed an upregulation of MYL7 (atrial myosin light chain 2, MLC2a) expression from day 20 to 40 which was not apparent in rectangular tissues (Supplementary Figure 4h).

Rectangular tissues show less spatial heterogeneity compared to microisland and square tissues.

By day 40 post differentiation, an outer tissue ring formed on both microisland and square tissue edges leaving the middle of the tissues less dense, while rectangles showed minimal areas of low

cell density (Figure 4a). To visualize the features of CMs inside the ECTs, whole tissue immunostaining was performed using alpha sarcomeric actinin ( $\alpha$ SA), connexin 43 (Cx43), and Hoechst (Figure 4b). Tissues from each geometry displayed similar bulk tissue characteristics on the tissue edge. The distribution of cells throughout tissue culture showed spatial heterogeneity between the center and edge of the tissue. To quantify this heterogenous fraction in each tissue geometry, total tissue area was manually measured from phase contrast images on day 20 and 40. Next, the heterogenous region inside the tissue was measured and divided by the total tissue area resulting in a fraction from 0 to 1. Rectangular tissues showed less regional heterogeneity on day 20 compared to their time-matched microisland tissue and on day 40 compared to square tissues (day 20: MI  $0.4 \pm 0.2$ , SQ  $0.32 \pm 0.11$ , RT  $0.20 \pm 0.10$ ; day 40 MI  $0.24 \pm 0.11$ , SQ  $0.27 \pm 0.08$ , RT  $0.17 \pm 0.09$ ) (Figure 4c).

All tissue geometries contract at similar frequencies and velocities at late timepoints.

Spontaneous contraction was recorded on days 20 and 40 and were analyzed using an open-source MATLAB code (20). Whole tissue averages were calculated by taking the average of several regions per tissue in each geometry. Frequency of contraction increased for all geometries from day 20 to day 40 (Figure 5a). The time interval between contraction and relaxation was significantly longer in square and rectangular tissues on both day 20 and 40 (Figure 5b). On day 20, contraction and relaxation velocity was significantly slower in rectangles compared to microislands (Figure 5 c, d), but these differences were not apparent by day 40. On day 40, the frequency, contraction velocity, and relaxation velocity increased for all geometries as expected with prolonged culture time.

Rectangular tissues show unidirectional contraction.

While tissue geometries contracted at similar frequencies, the qualitative videos showed differences in the way the different geometries contracted (Supplementary Movies 1, 2, 3). Microisland and square tissues contracted from the dense outer band inward towards the center of the tissue in all directions. The rectangular tissues contracted along their longitudinal axis. To quantify this, velocity vectors of spontaneous contraction were analyzed on day 40. Frames of a maximum contraction and maximum relaxation were superimposed with their vector fields (Figure 6a, red lines). These images were then used to create histograms for the frequency of each angle. Histograms for microisland and square geometries showed no major peaks corresponding to a single directionality (Figure 6c). Rectangular geometries demonstrated a single peak at  $45^{\circ}$  which corresponded with the longitudinal length of the tissue. Goodness of fit values for each histogram confirmed that the rectangular geometry had significantly more uniform contraction directionality compared to both microisland and square geometries (MI  $0.28 \pm 0.03$ , SQ  $0.35 \pm 0.05$ , RT  $0.79 \pm 0.04$ ), where 0 represents no fit and 1 represents a perfect fit (Figure 6b). Similar to the native myocardium, the rectangular tissue showed anisotropic contraction along the longitudinal axis.

*Square and Rectangular 3D-ECTs show more mature structural features.* 

3D-ECTs were dissociated and plated on fibronectin coated coverslips for single cell analysis. To visualize sarcomeres and gap junction proteins, dissociated cells were stained with αSA, Cx43, and Hoechst (Figure 7a). Sarcomeres were ~1.8 μm in length, agreeing with literature values for hiPSC-CMs (8), and showed no significant difference between tissue geometries. To further visualize ultrastructural features, TEM imaging was performed on day 140 samples (Figure 7b). These images revealed potential signs of higher maturation in square and rectangular tissues including sarcomeres with regularly spaced Z bands and adjacent mitochondria compared to

microisland tissue which presented with an immature arrangement of myofibrils and mitochondria with rudimentary sarcomere structures containing Z bodies.

Rectangular 3D-ECTs show increasing trend of conduction velocity with increased external pacing.

To assess electrophysiological responses, microisland and rectangle 3D-ECTs were optically mapped. 3D-ECT spontaneous depolarization rates were  $0.84 \pm 0.04$  Hz for MI and  $0.72 \pm 0.01$  Hz for RT. 3D-ECTs for both geometries exhibited 1:1 capture during external pacing up to 4 Hz. During spontaneous depolarization, calcium transient durations at 50% (CTD50) and 80% (CTD80) repolarization for MI were  $397 \pm 10$  ms and  $698 \pm 27$  ms and for RT they were  $394 \pm 19$  ms and  $716 \pm 19$  ms, respectively (Figure 8 a-c, n = 3 tissues). Calcium transient velocities were  $4.2 \pm 2.8$  cm/s for MI and  $7.2 \pm 2.2$  cm/s for RT (Figure 8 d, n = 3 tissues).

When 3D-ECTs were electrically paced at 1.0, 1.5, 2.0, 3.0, and 4.0 Hz, the CTD50 were 427  $\pm$  67, 326  $\pm$  19, 248  $\pm$  3, 154  $\pm$  13, 104  $\pm$  4 ms, respectively, for MI and 397  $\pm$  22, 341  $\pm$  14, 257  $\pm$  23, 162  $\pm$  2, 109  $\pm$  17 ms for RT. The CTD80 were 698  $\pm$  27, 688  $\pm$  53, 501  $\pm$  22, 360  $\pm$  9, 223  $\pm$  17, 164  $\pm$  10 ms for MI and 658  $\pm$  13, 513  $\pm$  5, 366  $\pm$  24, 221  $\pm$  5, 158  $\pm$  29 ms for RT (Figure 8 a and b, n = 3 tissues). Calcium transient velocities for MI 3D-ECTs were 3.5  $\pm$  1.5, 3.7  $\pm$  1.6, 3.6  $\pm$  1.2, 2.0  $\pm$ 1.3 cm/s for 1.0, 1.5, 2.0, and 3.0 Hz pacing, respectively; RT calcium transient velocities were 4.0  $\pm$  1.5, 6.0  $\pm$  2.8, 4.8  $\pm$  2.5, 7.9  $\pm$  6.7 cm/s (Figure 8 d, n = 3 tissues). In both cases, calcium transient velocities for 4 Hz recordings were unable to be accurately analyzed.

## **Discussion**

In this work, we produced 3D-ECTs in three tissue geometries and investigated the impact of initial tissue geometry on cardiac differentiation, maturation, and functionality. The hybrid biomaterial, PEG-fibrinogen, was selected to provide the 3D microenvironment based on its relevance in clinical trials (21) and previously published work. Previous microisland studies using

both PEG-fibrinogen (17) and GelMA (18) produced functional cardiac tissues that presented with adultlike ultrastructural features including T-tubules adjacent to Z lines and appropriate responses to external stimuli. While these studies provided vital foundational information, the microisland tissue geometry (diameter  $\sim 4$  mm) resulted in a dense outer ring of contracting tissue with a less viable tissue center.

To alleviate regional tissue heterogeneity and improve cardiac tissue maturation, here two new encapsulation geometries were investigated. The square geometry provided a straight edge for cell alignment while maintaining similar edge to center (roughly 4x4 mm) distances as the microisland. The rectangular geometry was designed to mimic a straightened version of the dense outer ring formed in the microisland tissues (1.5x5 mm). All three tissue geometry designs maintained the same initial tissue volume, cell density, and tissue thickness. HiPSCs were encapsulated in PEGfibrinogen in each of the three initial tissue geometries on acrylated glass coverslips and differentiated, forming spontaneously contracting 3D-ECTs by day 7. The similarities in differentiation efficiency, gene expression, and contraction velocity between geometries were well supported by the observation that each of these characterization methods is primarily assessing the properties of the dense outer band of cardiac tissue, which contains many more cells than the middle of the microisland and square 3D-ECTs. Early timepoint characterization including day 10 cardiac differentiation efficiency and gene expression showed that initial encapsulation geometry does not impact whether successful cardiac differentiation occurs. Differentiation efficiency in all three tissue geometries was similar to values reported in the literature for direct cardiac differentiation of hiPSCs in 3D (17, 18, 22). While there was no difference in cardiac differentiation efficiency between geometries, current literature supports in situ formation of engineered cardiac tissues through 3D hiPSC cardiac differentiation over the use of predifferentiated cardiomyocytes for engineered tissue formation. Direct cardiac differentiation of hiPSCs to cardiac tissues results in high cell densities as cells continue to proliferate post-encapsulation and enables elimination of the CM dissociation step post-differentiation which disrupts important cellular connections (17, 22).

This study demonstrated differences in cardiomyocyte functionality in response to changes in initial hiPSC encapsulation geometry. Comparable percentages of CMs post-differentiation provided a baseline for evaluation of the impact of initial encapsulation geometry on cardiac tissue function and maturation with extended culture time. Further study is warranted to provide additional insights, including in-depth analysis to assess potential differences in the non-cardiomyocyte, cTnT negative cell populations. Since differences in the efficiency of differentiation were not identified, evaluation here did not focus on the impact of tissue geometry on shorter-term key milestones of differentiation. Rather, the important differences in cardiac tissue maturation and functionality were observed at later timepoints between tissues geometries when tissues were cultured long term (30-150 days) as evidenced by reduced tissue heterogeneity and enhanced myofibrillar organization.

Enhanced maturation is critical for applications in pharmaceutical development and regenerative medicine. Unfortunately, most engineered cardiac tissue never progresses beyond the fetal developmental milestones, limiting its applicability in preclinical studies and cell therapy. Several methods of varying complexity have been utilized to enhance maturation, including but not limited to, altering substrate stiffness, contact guidance through micropatterning, electrical and mechanical stimulation (23). Plating CMs on stiffer substrates (up to 10kPa) has been shown to increase CM force generation and improve calcium handling (24). Similarly, seeding CMs on nanopatterned (25) micropatterned (26) surfaces has been shown to improve CM function and myofibrillar

alignment by mimicking nanoscale cues seen in native ECM and the microscale cues seen in myocardial architecture. While these methods are applicable to pre-differentiated CM monolayers, they are not relevant for 3D engineered cardiac tissue maturation that is composed of several layers of CMs. Introduction of intermittent electrical (27) and/or mechanical (28, 29) stimulation post differentiation has been shown to improve cardiac electrophysiology and increase myofibril alignment over time in 3D engineered tissues. However, these methods sacrifice simplicity for enhanced maturation which may not enable for widespread acceptance in cardiac tissue engineering and pharmaceutical testing applications. Here by modulating the initial geometry of hiPSC-laden, engineered tissues prior to cardiac differentiation, developing cardiomyocytes in the rectangular tissues experience both contact guidance as a result of the macroscale tissue axis and then starting on approximately differentiation day 10 aligned mechanical stimulation as a result of endogenous tissue contraction. The developing engineered cardiac tissues are crosslinked to the acrylated glass coverslips, which provide resistance during this aligned contraction in a manner potentially similar to systems that employ posts or pillars. Results show that functional cardiac maturation can be improved by simply using a rectangular tissue geometry during the initial hiPSC encapsulation step, rather than implementing cell selection or tedious post-differentiation manipulation.

Overall increased tissue homogeneity was consistently seen in the rectangular geometry compared to the microisland and square geometries. During initial stages of cardiac differentiation, we saw a change in viable cell density distribution from day -2 to day 7. On day -2, all tissue geometries showed uniform viable cell density distribution at both the edge and middle of hiPSC laden hydrogels. By day 0, hiPSCs colonies increased in size and remained evenly distributed throughout the hydrogels. After cardiac differentiation on day 7, there were regional differences

in viable cell density for all tissue geometries. The exact causes of regional viable cell distributions are unknown; cells in the center may have died or migrated to the outer edge where they have greater access to nutrients and waste removal (30). Due to the inherent nature of the rectangular geometry, where the middle is never as far from the edge compared to square and microisland geometries, regions of low viable cell density were smaller resulting in more homogenous cardiac tissues over time. Tissue homogeneity is important for studying the impact of therapeutics on cardiac electrophysiology, where anomalies in cardiac tissue can result in unwanted arrhythmias and disruptions in electrical signal propagation. To further refine tissue production and alleviate these areas of low viable cell density, additional testing could be performed to produce tissues with smaller dimensions to avoid nutrient diffusion limitations, or vasculature could be incorporated to improve oxygen and nutrient distribution and waste removal (31). While these methods add varying levels of complexity beyond the scope of this study, the knowledges gained would further narrow the focus for optimal cardiac tissue production for enhancing maturation.

Throughout long-term culture, tissue contraction progressed from initially localized areas of spontaneous beating to strong synchronous beating as the cardiac tissue became more interconnected in late-stage differentiation and maturation. Significant increases in contraction frequency and velocity were quantified from day 20 and day 40. While ECTs from each geometry contracted at similar speeds, the directionality of propagation was significantly different between geometries. Microisland and square ECTs contracted from their outer edges inward, toward the center of the tissue, potentially indicating CM alignment from the periphery into the middle of the tissue. Conversely, rectangular ECTs propagated along the longitudinal axis, indicating anisotropic CM alignment and contraction propagation. In addition, TEM imaging revealed higher myofibrillar organization and Z line formation in rectangular tissues compared to microislands.

The late time point of Day 140 was selected to align with prior TEM analysis of the microisland geometry, which had shown evidence of T-tubule formation (17). Given limitations at the time of this study, additional evaluation was not possible. Future study to evaluate potential geometry dependent differences in the timeline and extent of structural maturation is warranted. Both microisland and rectangular 3D-ECTs showed uniform calcium propagation as shown in the representative isochrone maps. 3D-ECTs appropriately responded to point electrical stimulation up to 4 Hz at 20 V (32, 33). Optical mapping data showed a higher calcium propagation frequency for microisland compared to rectangular for spontaneous activity which matches the higher contraction frequency for microisland. No other significant difference between geometries for CTD50, CTD80, and CV for the spontaneous activity or electrical pacing was observed. Calcium transient duration for both microisland and rectangular 3D-ECTs were compatible with other hiPSC-CMs results (CTD 50) at 1 Hz stimulation (~340 ms); however, exhibited higher CTD50 compared to human adult CMs (~250 ms) (34). Nevertheless, CV in rectangular tissues showed an increasing trend with increased frequency of external pacing which may be a sign of advancing maturity compared to microisland. Taken together, these findings demonstrate that encapsulating and differentiating hiPSCs in a rectangular geometry will result in more mature ECTs, with contractile and structural properties that more closely mimic native myocardium.

The approach presented here is relatively straight-forward to implement and has several advantages for producing 3D ECTs *in vitro*. However, making more intricate tissue geometries or utilizing additional cell types requires more complex solutions like bioprinting. First, the ability to 3D print positive casts for producing custom made PDMS molds allows for virtually unlimited design options for PDMS mold preparation. However, we are currently limited in tissue complexity by pipetting the polymer precursor solution by hand. Rudimentary geometries like

microisland, squares, and rectangles are easily pipetted by hand, but achieving even polymer

precursor distribution and tissue thickness in complex geometries is challenging. Bioprinting of

3D ECTs shows great potential for solving this problem where tissue can be printed with sub-

millimeter resolution (22). Second, while encapsulating hiPSCs on acrylated glass coverslips

enables ease of characterization and is likely important in the observed improved cardiac

maturation, it adds a limitation for tissue size and thickness. The acrylated coverslip prevents

nutrient and waste diffusion from the bottom surface area of the tissue; this most likely contributes

to the low viability in the center of microisland and square tissues.

Conclusions

In this study, we demonstrate the ability to impact cardiac tissue functionality by changing the

initial encapsulation geometry of hiPSCs in hydrogel biomaterials. Rectangular 3D-ECTs

displayed increased tissue uniformity with unidirectional contraction and evenly spaced and

aligned sarcomeres, which are hallmarks of native adult myocardium. This robust yet simple

encapsulation platform has the potential to be used in a range of applications including cardiac

drug development and cardiotoxicity analysis.

**AUTHOR INFORMATION** 

**Corresponding Author** 

\*Corresponding author: elipke@auburn.edu

**Author Contributions** 

The manuscript was written through contributions of all authors. All authors have given approval

to the final version of the manuscript.

**Funding sources:** National Institutes of Health UL1TR003096, the Department of Education GAANN #P200A150075 and #P200A180087, National Science Foundation NSF-CBET-1743445, Auburn University Undergraduate Research Fellowship, National Institutes of Health/NHLBI K01-HL133424 and R03- HL154286

#### ACKNOWLEDGMENT

The authors gratefully acknowledge Dr. Ronald Gordon, Department of Pathology at Icahn School of Medicine at Mount Sinai, for performing transmission electron microscopy.

## **ABBREVIATIONS**

3D-ECTs, three-dimensional engineered cardiac tissue; CM, Cardiomyocytes; COL3A1, Collagen Type III Alpha 1 Chain; cTnT, cardiac troponin T; Cx43, connexin 43; GJA5, Connexin 40, CX40; hiPSC, human induced pluripotent stem cell; hiPSC-CMs, hiPSC-derived cardiomyocytes; ID, intercalated disc; M, mitochondria; MLY2, ventricular myosin light chain 2, MLC2v; MYH6, α-myosin heavy chain, α-MHC; MYH7, β-myosin heavy chain, β-MHC; MYL7, atrial myosin light chain 2, MLC2a; NVP, N-vinylpyrrolidone; NZB, nascent Z band; PBS, Phosphate-Buffer Saline; PDMS, Polydimethylsiloxane; PEGDA, Poly (ethylene glycol) diacrylate; PEG-fibrinogen, poly (ethylene glycol) fibrinogen; ROI, Region of Interest; RT-qPCR, Reverse Transcription Quantitative PCR; TCEP-HCl, Tris (2-carboxyethyl) phosphine hydrochloride; TEM, transmission electron microscopy; TEOA, triethanolamine; ZB, Z-bands; αSA, alpha-sarcomeric actinin.

## REFERENCES

- 1. World health statistics 2017: monitoring health for the SDGs, Sustainable Development Goals. Geneva: World Health Organization. 2017.
- 2. Bernstein HS. Tissue engineering in regenerative medicine. New York: Humana Press,; 2011.
- 3. Takahashi K, Tanabe K, Ohnuki M, et al. Induction of pluripotent stem cells from adult human fibroblasts by defined factors. Cell. 2007;131(5):861-72.
- 4. Yang L, Soonpaa MH, Adler ED, et al. Human cardiovascular progenitor cells develop from a KDR+ embryonic-stem-cell-derived population. Nature. 2008;453(7194):524-8.
- 5. Kattman SJ, Witty AD, Gagliardi M, et al. Stage-specific optimization of activin/nodal and BMP signaling promotes cardiac differentiation of mouse and human pluripotent stem cell lines. Cell Stem Cell. 2011;8(2):228-40.
- 6. Lian X, Zhang J, Azarin SM, et al. Directed cardiomyocyte differentiation from human pluripotent stem cells by modulating Wnt/beta-catenin signaling under fully defined conditions. Nat Protoc. 2013;8(1):162-75.

- 7. Burridge PW, Thompson S, Millrod MA, et al. A Universal System for Highly Efficient Cardiac Differentiation of Human Induced Pluripotent Stem Cells That Eliminates Interline Variability. Plos One. 2011;6(4).
- 8. Feric NT, Radisic M. Maturing human pluripotent stem cell-derived cardiomyocytes in human engineered cardiac tissues. Adv Drug Deliv Rev. 2016;96:110-34.
- 9. Chen HS, Kim C, Mercola M. Electrophysiological challenges of cell-based myocardial repair. Circulation. 2009;120(24):2496-508.
- 10. Black LD, Meyers JD, Weinbaum JS, et al. Cell-Induced Alignment Augments Twitch Force in Fibrin Gel-Based Engineered Myocardium via Gap Junction Modification. Tissue Eng Pt A. 2009;15(10):3099-108.
- 11. Chung CY, Bien H, Entcheva E. The role of cardiac tissue alignment in modulating electrical function. J Cardiovasc Electrophysiol. 2007;18(12):1323-9.
- 12. Kleber AG, Rudy Y. Basic mechanisms of cardiac impulse propagation and associated arrhythmias. Physiol Rev. 2004;84(2):431-88.
- 13. Severs NJ. The cardiac muscle cell. Bioessays. 2000;22(2):188-99.
- 14. Trantidou T, Terracciano CM, Kontziampasis D, et al. Biorealistic cardiac cell culture platforms with integrated monitoring of extracellular action potentials. Scientific reports. 2015;5.
- 15. Kim DH, Lipke EA, Kim P, et al. Nanoscale cues regulate the structure and function of macroscopic cardiac tissue constructs. P Natl Acad Sci USA. 2010;107(2):565-70.
- 16. McDevitt TC, Angello JC, Whitney ML, et al. In vitro generation of differentiated cardiac myofibers on micropatterned laminin surfaces. Journal of Biomedical Materials Research. 2002;60(3):472-9.
- 17. Kerscher P, Turnbull IC, Hodge AJ, et al. Direct hydrogel encapsulation of pluripotent stem cells enables ontomimetic differentiation and growth of engineered human heart tissues. Biomaterials. 2016;83:383-95.
- 18. Kerscher P, Kaczmarek JA, Head SE, et al. Direct Production of Human Cardiac Tissues by Pluripotent Stem Cell Encapsulation in Gelatin Methacryloyl. ACS Biomaterials Science & Engineering. 2016;3(8):1499-509.
- 19. Dikovsky D, Bianco-Peled H, Seliktar D. The effect of structural alterations of PEG-fibrinogen hydrogel scaffolds on 3-D cellular morphology and cellular migration. Biomaterials. 2006;27(8):1496-506.
- 20. Huebsch N, Loskill P, Mandegar MA, et al. Automated Video-Based Analysis of Contractility and Calcium Flux in Human-Induced Pluripotent Stem Cell-Derived Cardiomyocytes Cultured over Different Spatial Scales. Tissue Eng Part C-Me. 2015;21(5):467-79.
- 21. Fuoco C, Salvatori ML, Biondo A, et al. Injectable polyethylene glycol-fibrinogen hydrogel adjuvant improves survival and differentiation of transplanted mesoangioblasts in acute and chronic skeletal-muscle degeneration. Skelet Muscle. 2012;2(1):24.
- 22. Kupfer ME, Lin WH, Ravikumar V, et al. In Situ Expansion, Differentiation and Electromechanical Coupling of Human Cardiac Muscle in a 3D Bioprinted, Chambered Organoid. Circ Res. 2020.
- 23. Yang X, Pabon L, Murry CE. Engineering adolescence: maturation of human pluripotent stem cell-derived cardiomyocytes. Circ Res. 2014;114(3):511-23.
- 24. Jacot JG, McCulloch AD, Omens JH. Substrate stiffness affects the functional maturation of neonatal rat ventricular myocytes. Biophys J. 2008;95(7):3479-87.
- 25. Kim DH, Lipke EA, Kim P, et al. Nanoscale cues regulate the structure and function of macroscopic cardiac tissue constructs. P Natl Acad Sci USA. 2010;107(2):565-70.

- 26. McDevitt TC, Angello JC, Whitney ML, et al. In vitro generation of differentiated cardiac myofibers on micropatterned laminin surfaces. J Biomed Mater Res. 2002;60(3):472-9.
- 27. Tandon N, Cannizzaro C, Chao PH, et al. Electrical stimulation systems for cardiac tissue engineering. Nat Protoc. 2009;4(2):155-73.
- 28. Ge D, Liu X, Li L, et al. Chemical and physical stimuli induce cardiomyocyte differentiation from stem cells. Biochem Biophys Res Commun. 2009;381(3):317-21.
- 29. Gelmi A, Cieslar-Pobuda A, de Muinck E, et al. Direct Mechanical Stimulation of Stem Cells: A Beating Electromechanically Active Scaffold for Cardiac Tissue Engineering. Adv Healthc Mater. 2016;5(12):1471-80.
- 30. Radisic M, Malda J, Epping E, et al. Oxygen gradients correlate with cell density and cell viability in engineered cardiac tissue. Biotechnol Bioeng. 2006;93(2):332-43.
- 31. Radisic M, Yang L, Boublik J, et al. Medium perfusion enables engineering of compact and contractile cardiac tissue. Am J Physiol Heart Circ Physiol. 2004;286(2):H507-16.
- 32. Shadrin IY, Allen BW, Qian Y, et al. Cardiopatch platform enables maturation and scale-up of human pluripotent stem cell-derived engineered heart tissues. Nat Commun. 2017;8(1):1825.
- 33. Bursac N, Parker KK, Iravanian S, et al. Cardiomyocyte cultures with controlled macroscopic anisotropy: a model for functional electrophysiological studies of cardiac muscle. Circ Res. 2002;91(12):e45-54.
- 34. Pioner JM, Santini L, Palandri C, et al. Optical investigation of action potential and calcium handling maturation of hiPSC-cardiomyocytes on biomimetic substrates. International journal of molecular sciences. 2019;20(15):3799.

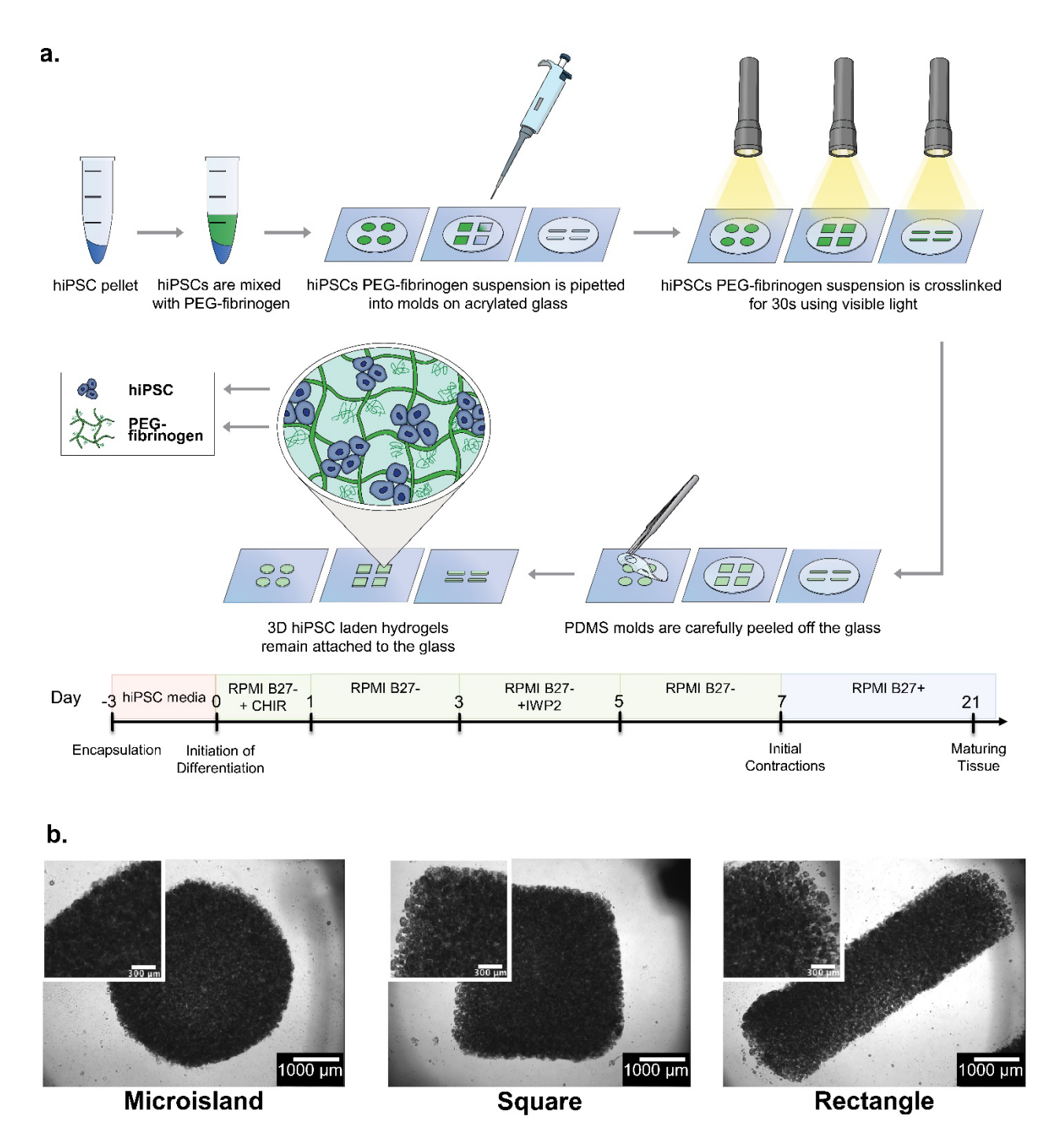


**Figure 1.** HiPSCs were encapsulated and differentiated in microisland, square, and rectangular geometries. (a) To immobilize tissues hiPSCs were encapsulated in PEG-fibrinogen hydrogels on acrylated glass coverslips. Maintaining equivalent volume and thickness, three tissue geometries were produced using custom microisland, square, and rectangle PDMS molds. (b) HiPSC colonies

were evenly distributed throughout each tissue geometry as shown in day -2 phase contrast images. Resulting tissues were cultured in stem cell media for three days prior to cardiac differentiation beginning on day 0.

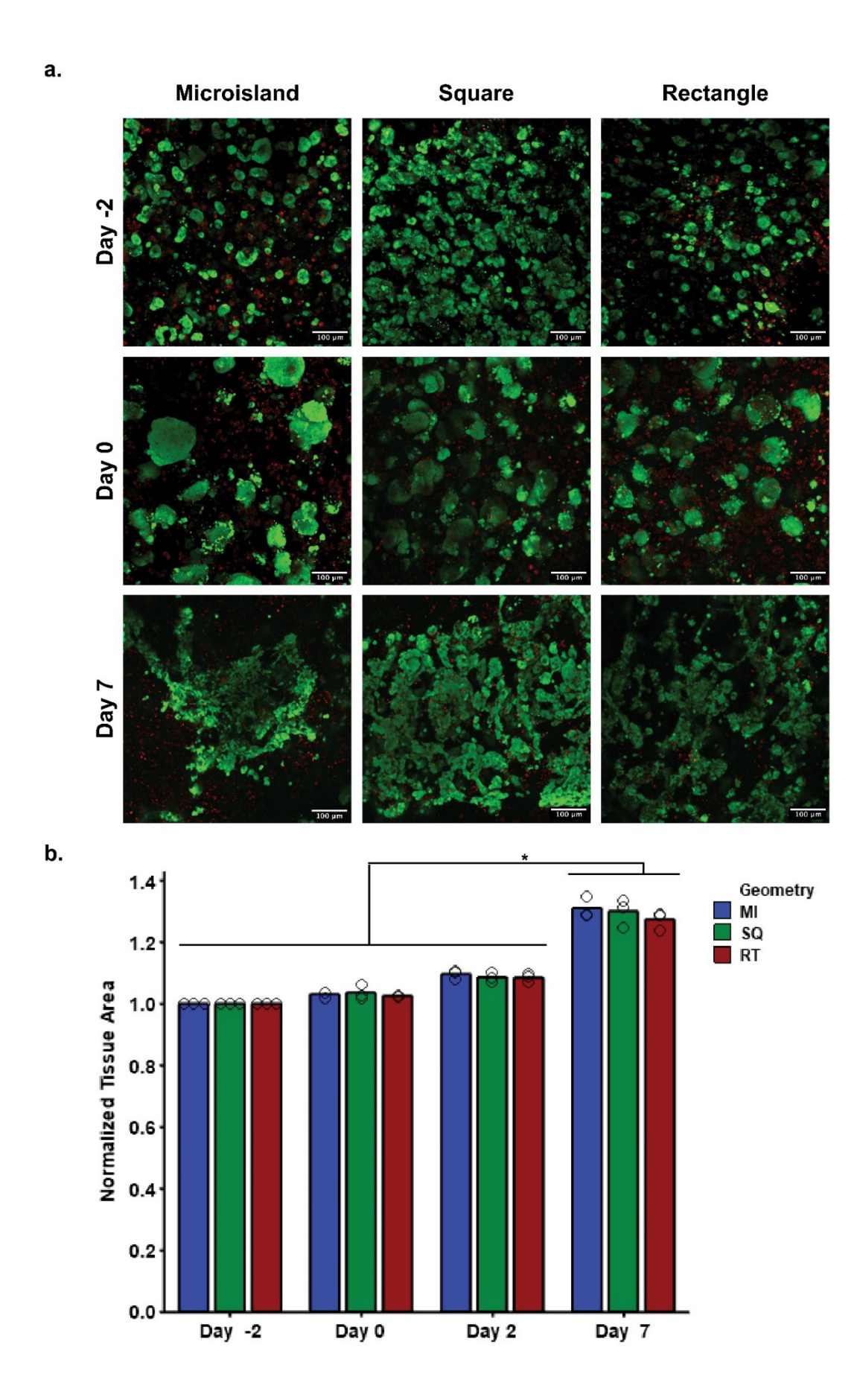


**Figure 2.** HiPSC colonies remained viable and grew in the 3D PEG-fibrinogen microenvironment post-encapsulation. (a) Viable cell density was evenly distributed throughout the tissue edge in all geometries on day -2. From day -2 to the onset of differentiation on day 0, viable cell colonies increased in size and maintained an even distribution. By day 7 of differentiation, viable cell colonies localized toward the edge of both microisland and square tissue geometries (Supplementary Figure 3), while maintaining a nearly even distribution throughout the rectangular tissues. (b) 3D-ECTs from all geometries maintained a similar size throughout differentiation with all tissue types increasing by 30% by day 7 (Live-green, Dead-red, n = 3 encapsulations containing 4 tissues each from each geometry per timepoint, circles represent an average of 4 tissues per encapsulation and bar reports mean for 3 encapsulations, \* p < 0.05)

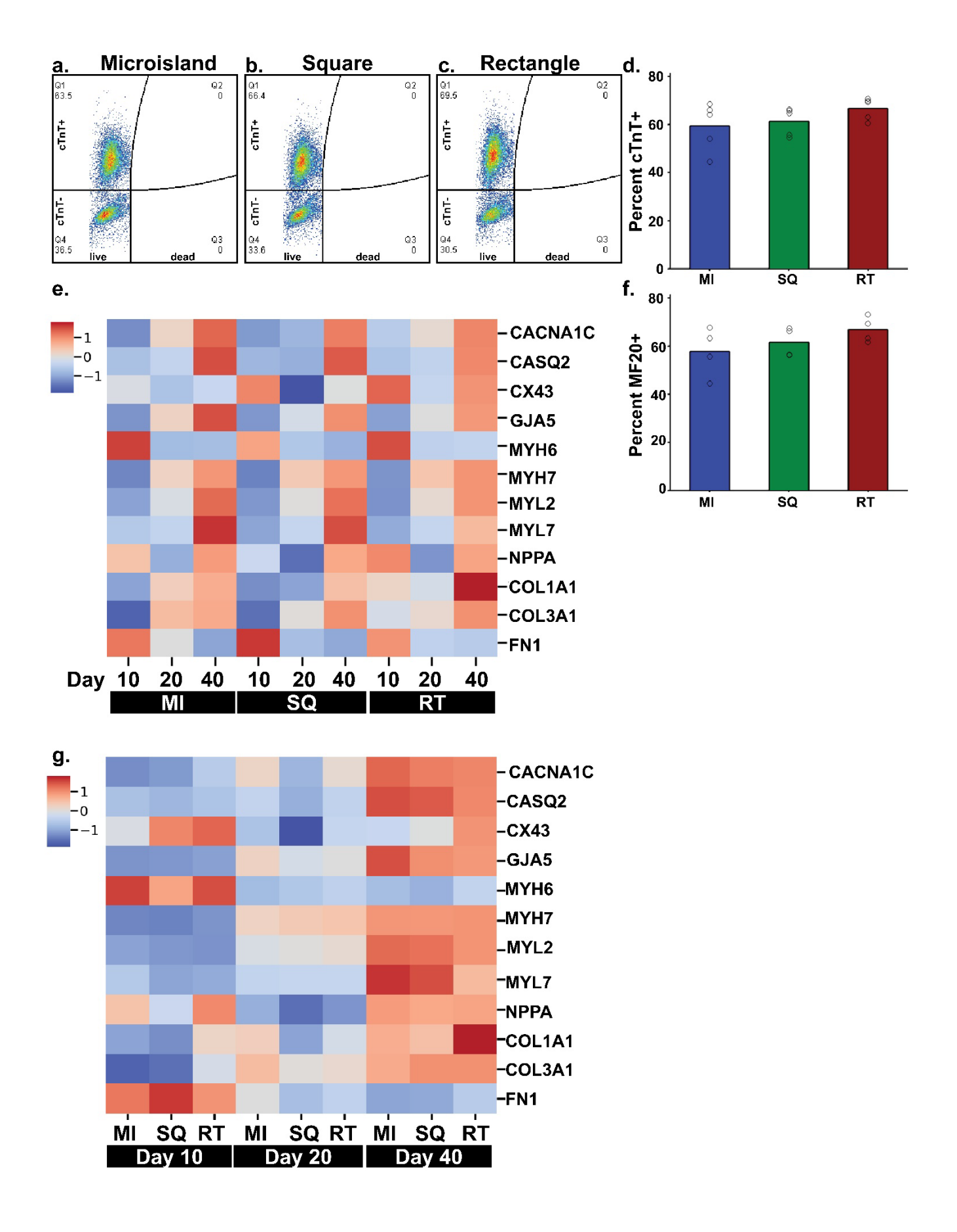


**Figure 3.** HiPSCs differentiated in all tissue geometries and showed temporally appropriate changes in gene expression. (a-c) Representative dot-plots show live single cells gated for cTnT+. (d,f) Microisland, square, and rectangular tissues contained 59.5%, 61.4%, and 66.7% cTnT positive populations and 57.9%, 61.7%, and 67.0% MF20 positive populations respectively (n = 3 differentiations, 2 tissues from each differentiation for each geometry, mean  $\pm$  s.d.). Heat maps compare various cardiac maturation and ECM-related genes for (e) each geometry overtime and (g) each geometry at each timepoint. (n = 3 samples per geometry per timepoint, data is normalized to GAPDH, blue colors correspond to an upregulation, red colors correspond to a downregulation, individual gene data in Supplementary Figure 4).

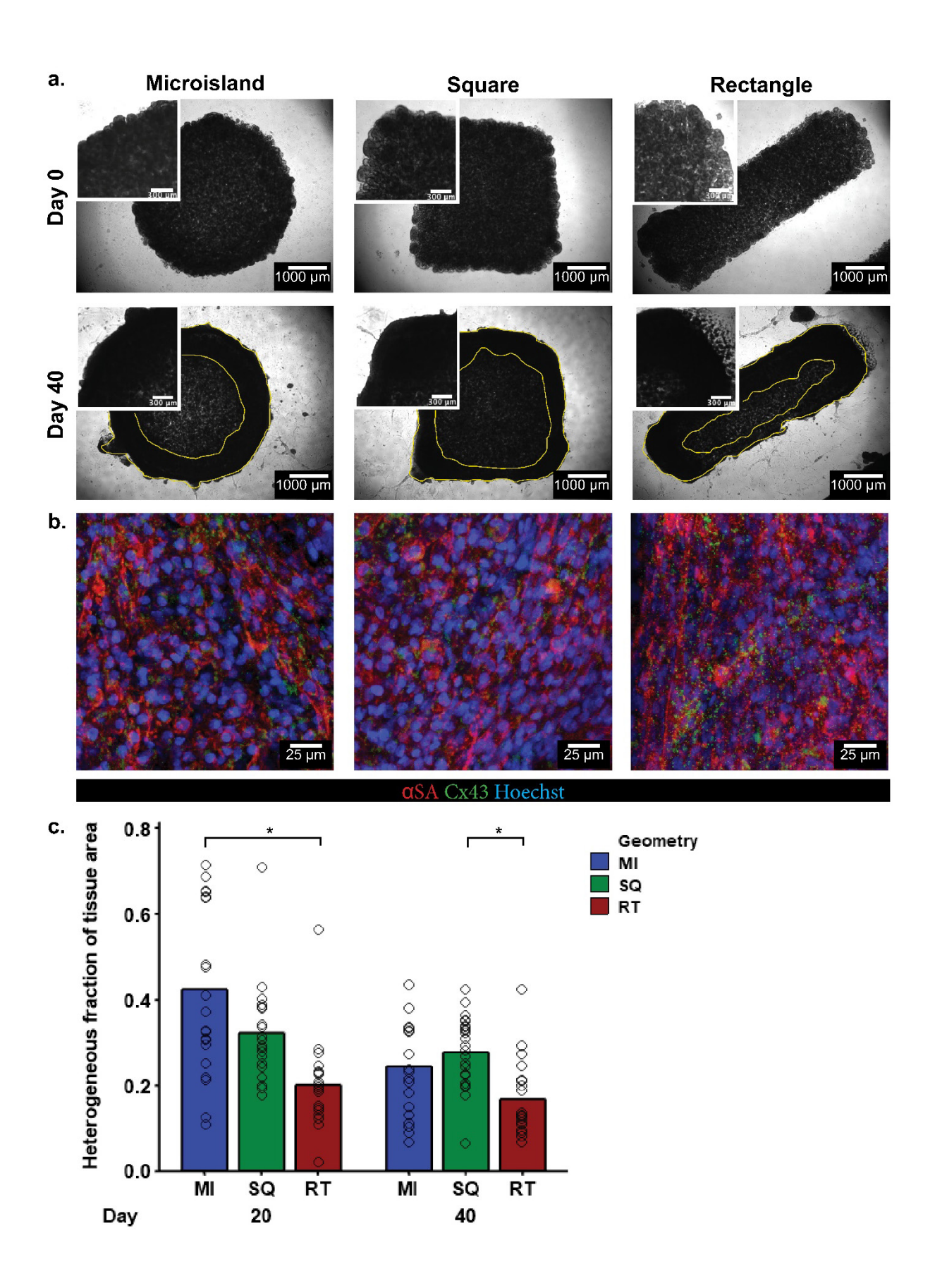


**Figure 4.** HiPSCs in 3D-ECTs underwent successful cardiac differentiation and remodeled their microenvironment over time. (a) HiPSC encapsulation resulted in homogenous cell distribution on day 0. After differentiation, dense outer rings formed on microisland and square geometries, which were less apparent in rectangular tissues (outlined in yellow). (b) Whole 3D-ECTs samples from each geometry show the high incidence of cardiomyocytes with positively stained sarcomeres (αSA, red ) and gap junction protein, connexin 43 (Cx43, green) on the edge of each tissue. (c) Regions of tissue heterogeneity were identified and measured with Image J, and then divided by total tissue area to calculate the heterogenous fraction of tissue area. Rectangular tissues show significantly less heterogeneity compared to microislands on day 20 and squares on day 40 (circles indicate individual tissues, bar indicates average, n> 15 tissue per geometry at each timepoint, \* p < 0.05).

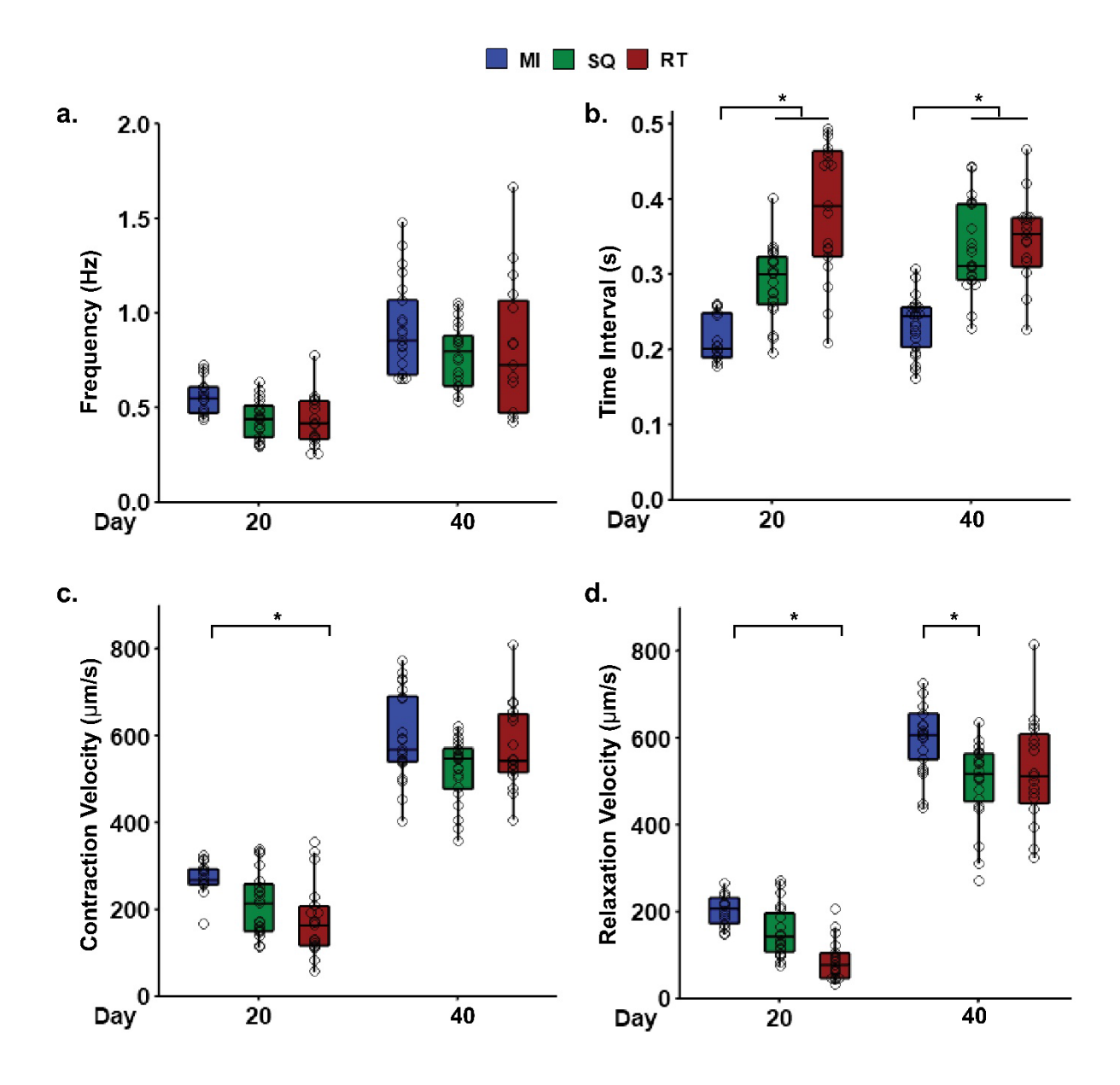


**Figure 5.** ECTs exhibited an increase in contraction velocity with tissue development in all geometries. (a, c, d) Contraction analysis of ECTs indicated an increase of contraction frequency, contraction velocity, and relaxation velocity with culture time for all geometries. (b) Time interval between contraction and relaxation was significantly higher in square and rectangular tissue compared to microislands at each time point. Each data point represents the average value of

multiple regions of interest per 3D-ECT. (n = 5 encapsulations, 4 tissue per encapsulation per geometry, \* p < 0.05)

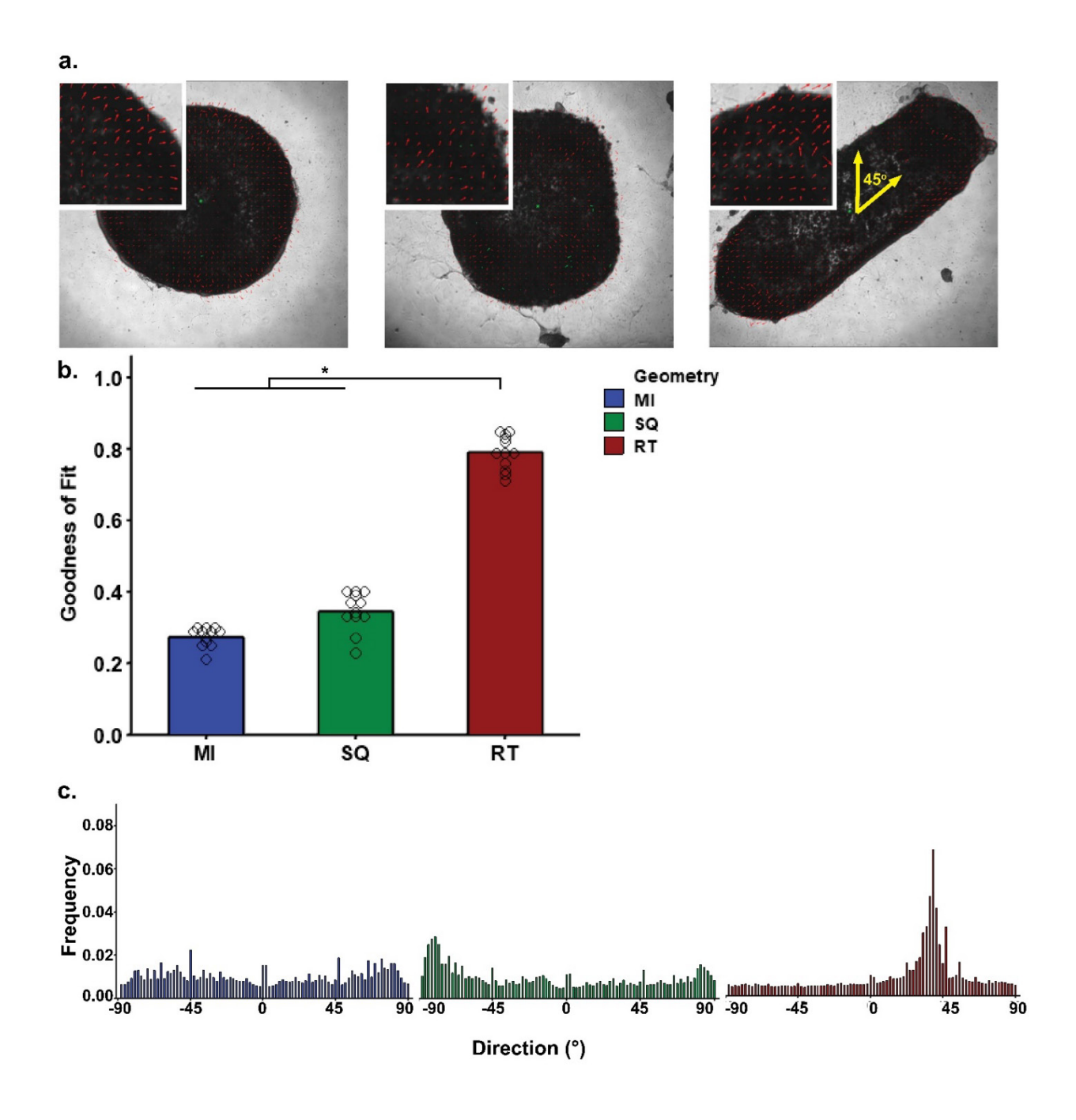


**Figure 6.** Rectangular ECTs exhibited anisotropic contraction along a longitudinal axis whereas the other geometries did not. (a) ECT velocity vector (red lines) fields were analyzed to give frequencies of contraction vectors at angles from -90° to 90°. (c) Microisland and square geometries had roughly zero directionality around the center of beating, while rectangular

geometries exhibited a peak of contraction at  $45^{\circ}$ , corresponding to the longitudinal axis. (b) Goodness of fit values show microisland and square geometries had significantly lower directionality, where 0 represents no single directionality and 1 represents a single directionality. (n = 5 encapsulations, 4 tissues per encapsulation per geometry, for each geometry at each timepoint, mean  $\pm$  s.d., p < 0.05)

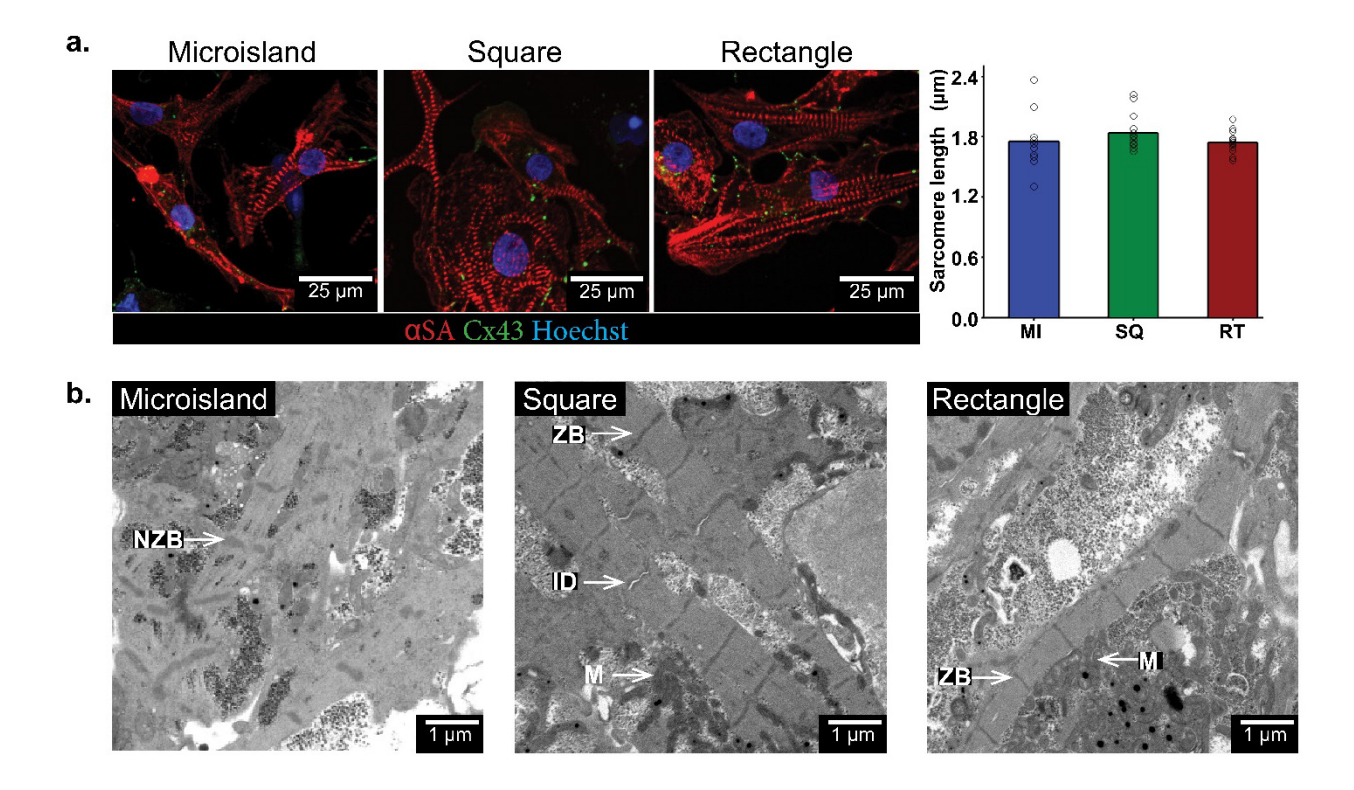


**Figure 7.** Rectangle and square 3D-ECTs show features of advancing maturity compared to microislands. 3D-ECTs from each geometry were dissociated, plated on coverslips, and immunostained for sarcomere quantification ( $\alpha$ SA-red, Cx43-green, Hoechst-blue). (a) No significant difference in sarcomere length was observed between the three geometries with average lengths of 1.75, 1.84, and 1.74 microns for CMs from microislands, squares, and rectangles, respectively. (n>10 CMs per geometry, mean  $\pm$  s.d., p < 0.05) (b) TEM images from late timepoint 3D-ECTs show poorly organized nascent z-bodies in microisland tissue compared to regularly spaced Z bands in square and rectangular tissues (n= 3 tissue per geometry, NZB: nascent Z band, ZB: Z-bands, ID: intercalated disc, M: mitochondria).

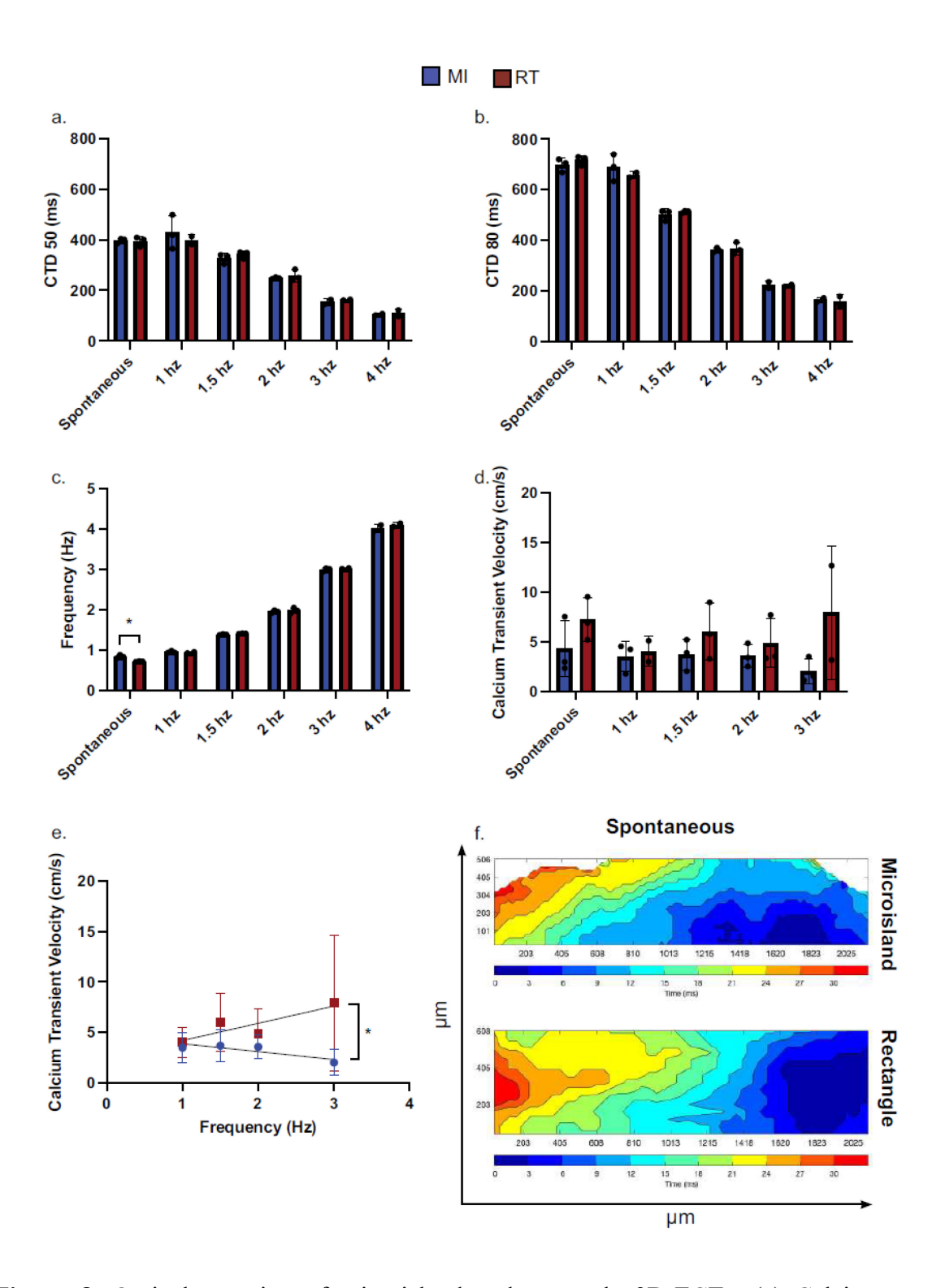


**Figure 8**. Optical mapping of microisland and rectangle 3D-ECTs. (a) Calcium transient duration (CTD) at 50% and (b) 80% repolarization was quantified during spontaneous calcium

transient propagation and point electrical stimulation. Bar graphs of average CTD50 and CTD80 for both microisland (MI) and rectangle (RT) 3D-ECTs show a graded decrease in CTD with increasing external pacing frequency. No significant difference in CTD50 and CTD80 was observed between MI and RT 3D-ECTs. (c) Frequency of external pacing versus the frequency of calcium transient propagation. (d) Calcium transient velocities for MI and RT 3D-ECTs. (e) An increasing trend of CV for RT tissue was observed by increasing the frequency of external pacing, which may be a sign of functional maturation. (f) Representative isochrone maps during spontaneous calcium propagation for MI (top) and RT (bottom) 3D-ECTs at day 35 of differentiation has been shown (n = 3 tissues, \* p<0.05)

# **Supplementary Information**

# **Supplementary Table 1.** Primers used for qPCR

Gene (Product)	Primers, F:Forward, R:Reverse, Pr:Probe (Taqman primers only)
CACNA1C (CaV1.2)	F: GGTCTTGATTTCAGAAGGAC
	R: CAGTTCACAAAGGGTAAGAG
CASQ2	F: GATCTAATTGAAGACCCAGTG
(Calsequestrin 2)	R: CACTCTTGAAAAAGCCAATG
COL1A1	F: GCTATGATGAGAAATCAACCG
(Collagen Type I alpha 1 chain)	R: TCATCTCCATTCTTTCCAGG
COL3A1	F: ATTCACCTACACAGTTCTGG
(Collagen Type III alpha 1 chain)	R: TGCGTGTTCGATATTCAAAG
GJA1	F: TGAGCAGTCTGCCTTTCGTT
(Cx43)	R: CCAGAAGCGCACATGAGAGA
	Pr: /56-FAM/ACACTCAGC/ZEN/AACCTGGTTGTGAAA/3IABkFQ/
FN1	F: CCATAGCTGAGAAGTGTTTTG
(Fibronectin)	R: CAAGTACAATCTACCATCATCC
GAPDH for SYBR Green	F: TCGGAGTCAACGGATTTG
	R: CAACAATATCCACTTTACCAGAG
GAPDH for Taqman	F: CCCCTTCATTGACCTCAACTACA
	R: TTGCTGATGATCTTGAGGCTGT
	P: /5Cy5/AAATCCCATCACCATCTTCCAGGAGC/3IAbRQSp/
GJA5	F: CCTCTACCCAGTATACGAAG
(Cx40)	R: GCTGGTATGTAGAGAGAGAG

MYH6	F: ACCAACCTGTCCAAGTTCCG
(aMHC)	R: TTGCTTGGCACCAATGTCAC
	Pr: /56-FAM/AGCATGAGC /ZEN/TGGATGAGGCAGAG /3IABkFQ/
MYH7	F: CACAGCCATGGGAGATTCGG
(βМНС)	R: CAGGCACGAAGACATCCTTCT
	Pr: /56-FAM/CCTACCTGC /ZEN/GCAAGTCAGAGAAGG /3IABkFQ/
MYL2	F: GGGCGGAGTGTGGAATTCTT
(MLC2v)	R: CCCGGCTCTCTTTGCTT
	Pr: /56-FAM/AGTGCTGGG /ZEN/TCCTTTCCACCAT /3IABkFQ/
MYL7	F: GTTCTTCCAACGTCTTTTCC
(MLC2a)	R: ATCACGATTCTGGTCGATAC
NPPA	F: GTACTGAAGATAACAGCCAG
(NPPA)	R: GATGTGAGAAGTGTTGACAG

# HiPSC Encapsulation Geometry Impacts 3D Developing Human Engineered Cardiac Tissue Functionality

Morgan E. Ellis<sup>1</sup>, Bryana N. Harris<sup>1</sup>, Mohammadjafar Hashemi<sup>1</sup>, B. Justin Harvell<sup>1</sup>, Michaela Z. Bush<sup>1</sup>, Emma E. Hicks<sup>1</sup>, Ferdous B. Finklea<sup>1</sup>, Eric M. Wang<sup>1</sup>, Ravikiran Nataraj<sup>1</sup>, Nathan P. Young<sup>1</sup>, Irene C. Turnbull<sup>2</sup>, Elizabeth A. Lipke<sup>1</sup>\*

# **Supplementary Methods**

Glass Acrylation and PDMS Mold Preparation

Tissues were immobilized on acrylated glass coverslips to accurately track tissue development.

Circular glass coverslips (21 mm, No.1 Fischer Scientific) were sterilized in 70% sulfuric acid

<sup>&</sup>lt;sup>1</sup> Department of Chemical Engineering, 212 Ross Hall, Auburn University, Auburn, AL 36849,

<sup>&</sup>lt;sup>2</sup>Cardiovascular Research Institute, Icahn School of Medicine at Mount Sinai, 1470 Madison Ave, New York, NY 10029

<sup>\*</sup> Corresponding author: Elizabeth A. Lipke, elipke@auburn.edu

(H<sub>2</sub>SO<sub>4</sub>) and 30 % hydrogen peroxide (H<sub>2</sub>O<sub>2</sub>) for approximately 30 minutes, rinsed with ethanol, and dried overnight in an oven at 40°C. Sterilized cover slips were added to acrylation solution containing 0.26 % (v/v) glacial acetic acid, 2.64% (v/v) distilled water, 0.48% (v/v) 3-(Trimethoxysilyl) propyl methacrylate, and 97% (v/v) ethanol for 12 hours at room temperature. After acrylation, coverslips were rinsed with ethanol, dried, and stored at 4 °C.

Polydimethylsiloxane (PDMS) molds were created using the Sylgard Elastometer Kit (Fisher Scientific) (Supplementary Figure 1). The Sylgard 184 curing agent was mixed with the Sylgard 184 silicone elastomer at a 1:10 ratio and placed under vacuum to remove bubbles. The mixture was poured into 3D printed negative castings of the desired tissue geometries and cured for 48 hours at room temperature. After curing, the molds were peeled off the castings, sonicated in 70% ethanol solutions, and sterilized under ultraviolet light before use. For encapsulations, the PDMS molds were placed on top of an acrylated glass coverslip.

3D-printed cast were designed using SolidWorks software. Cast were printed using acrylonitrile butadiene styrene filament. The basic design was a round wafer shape with raised areas representing the negative volume of the desired tissue geometries. Square molds had a tissue 1:1 length to width ratio. Rectangular molds had a tissue 5:1 length to width ratio. PDMS molds were designed to achieve equivalent initial tissue thickness during cell seeding and biomaterial crosslinking. Microisland tissue served as the control.

#### HiPSC Culture

IMR90 clone 1 (WiCell) hiPSCs were cultured in mTeSR medium (Stem Cell Technologies) on six-well plates coated with hESC qualified Matrigel (BD Biosciences) at 37 °C, 5% CO<sub>2</sub>, and 85% relative humidity. HiPSCs were passaged approximately every 4 days using Versene for 4.5

minutes at 37 °C into mTeSR supplemented with 10 μM ROCK inhibitor (RI, Y-27632, Stem Cell Technologies) for 24 hours after passaging.

Synthesis of PEG-fibrinogen and Preparation of Precursor Solution

Poly (ethylene glycol) diacrylate (PEGDA) and poly (ethylene glycol) fibrinogen (PEG-fibrinogen) were synthesized as previously described (1, 2).

Briefly, acryloyl chloride was reacted with PEG (molecular weight: 10 kDa) in a 4:1 molar ratio in anhydrous dichloromethane with trimethylamine at 1:2 molar ratio under argon overnight at 25 °C. The reacted PEGDA mixture was purified by phase separation using 2M K<sub>2</sub>CO<sub>3</sub>. The synthesize PEGDA was dried using anhydrous MgSO<sub>4</sub> and filtered. Lastly, the PEGDA was precipitated in diethyl ether, filtered, and dried at room temperature overnight. The PEGDA was stored at -20 °C. ¹H NMR was used to calculate the degree of acrylation.

PEG-fibrinogen was synthesized by covalently coupling bovine fibrinogen to PEGDA. Bovine fibrinogen (7 mg/ml) was dissolved in 10 mM PBS containing 8 M urea solution. Tris (2-carboxyethyl) phosphine hydrochloride (TCEP-HCl) was added to the above solution in a 1.5:1 molar ratio of TCEP to fibrinogen cysteines. The pH was adjusted to 8.0. The synthesized PEGDA was dissolved in 8M urea-PBS solution at 280 mg/ml, centrifuged to form a clear solution, and added to the fibrinogen solution. The reaction proceeded for three hours in the dark at 25 °C and stopped by diluting the solution with an equal volume of 8M urea-PBS buffer. The reaction products were precipitated in acetone at a 4:1 volumetric ratio of acetone to product solution. After settling, the precipitate was centrifuged, and the supernatant was removed. The remaining product was weighed and dissolved in 8M urea-PBS buffer at a concentration of 2.2 mL of buffer/ gram of precipitate. Finally, the product was dialyzed against 1L of PBS at 4 °C in the dark overnight

and stored at -80 °C. PEG-fibrinogen protein content was measured using Pierce<sup>TM</sup> BCA Protein Assay Kit (Thermo Fisher Scientific). Relative PEGDA content was determined by aliquoting PEG-fibrinogen solution into glass vials, lyophilizing, and calculating the net weight of the dry solid.

The PEG-fibrinogen polymer precursor solution was made using PEG-fibrinogen at a final protein concentration of 10 mg/ml in PBS. The PEG-fibrinogen was combined with 1.5v/v% triethanolamine (TEOA), 0.39 v/v% N-vinylpyrrolidone (NVP) and 0.1 mM eosin Y (Fischer Scientific) photoinitiator.

#### Viability and Immunofluorescent Visualization

A viability assay was performed using Live/Dead Viability kit (Thermo Fisher Scientific). Whole 3D-ECTs were stained with calcein AM, ethidium homodimer-1, and Hoechst 33342 and visualized using a Nikon A1R laser-scanning confocal microscope. Confocal Z-stacks with 5 μm steps were taken at the edge and in the middle of each tissue geometry and projected to a single image.

### Early 3D-ECT Growth

Low magnification (2X) phase contrast images were taken of 3D-ECTs throughout differentiation on days -2, -1, 0, 2, and 7 using a Ti Eclipse Nikon equipped with an Andor Luca S camera. Images were processed using ImageJ. To quantify tissue area growth over time,  $(n \ge 3)$  encapsulations per time point for each geometry) tissue area was calculated for each tissue and normalized to itself on day -2. Regions of cellular distribution heterogeneity were quantified by subtracting the void regions from the total tissue area.

#### Tissue Dissociation

3D-ECTs were dissociated using collagenase type B (Worthington) and 0.025% trypsin (Corning). Tissues were washed with PBS and placed in 1mg/mL collagenase type B with 0.5 mg/mL DNAse solution for roughly 10 minutes in a 37°C water bath with periodic shaking. The samples were spun down, the supernatant was removed, and the cell pellets were resuspended in 0.025% trypsin for 2 minutes in a 37°C water bath. The trypsin solution was neutralized with three times the volume of RPMI20. The suspension was centrifuged, supernatant was removed, and cells were resuspended in PBS or media for further characterization.

#### Flow Cytometry

On day 10, 3D-ECTs (n = 3, 2 tissues per encapsulation for 3 encapsulations for each geometry) were dissociated as described above. Resulting cell pellets were washed with PBS before being labeled with the viability marker Zombie Green (Biolegends, Cat No. 423111, 1:1000) for 30 minutes. Cells were washed with 10% FBS with 1% BSA blocking buffer. The cells were centrifuged, the supernatant was removed, and the cells were resuspended in FoxP3 (Thermo Fisher Scientific) for fixation overnight at 4°C. The following day cells were permeabilized in Permeabilization Buffer (Thermo Fisher Scientific). Next, the cells were blocked and permeabilized using FACS buffer containing 10% FBS and 1% BSA in Permeabilization Buffer. Cell suspensions were filtered using 40 µm flow filters and split for primary staining. Cells were labeled with primary antibody MF 20 (Developmental Studies Hybridoma Bank, 1:200) or cardiac troponin T (cTnT, Thermo Fisher Scientific, Cat No. MA512960, 1:400) for one hour at room temperature and washed 3 times with Permeabilization Buffer. Cells were then incubated with

secondary antibody (Alexa Flour 647, Thermo Fisher Scientific, Cat No. A21235, 1:300) for 45 minutes at room temperature, washed three times with Permeabilization Buffer, and resuspended in blocking buffer for analysis. Samples were analyzed using a Cytoflex LX and FlowJo software. Data presented represents all live, single cells.

# Immunostaining and sarcomere length

To visualize differences in cardiac tissue formation and sarcomere length between geometries, immunostaining was performed using alpha-sarcomeric actinin (αSA, Sigma, A7811, 1:200), connexin 43 (Cx43, Sigma, Cat No. C6219, 1:100), and Hoechst 33342 (Sigma, Cat No. 382065, 1:3600). Whole tissues from each geometry were fixed with 2% paraformaldehyde, permeabilized using PBS-T, and blocked using 10% FBS with 1% BSA blocking buffer. Next tissues were incubated with primary antibodies at 4°C overnight, washed with PBS-T, and incubated with secondary antibodies (Alexa Fluor 488, Thermo Fisher Scientific, Cat No. A11008 and Alexa Fluor 568, Thermo Fisher Scientific, Cat No. A11004, 1:200) for 2 hours at room temperature. Immunostained tissue were imaged using Nikon A1R laser-scanning confocal microscope at 20X with 5 μm steps.

Dissociated cardiomyocytes were plated on fibronectin coated glass coverslips and immunostained with alpha-sarcomeric actinin (α-SA), connexin 43 (Cx43), and Hoechst 33342 to quantify sarcomere length. Images were taken at 40X magnification and sarcomere length was measured using ImageJ.

Contraction, directionality, and spatial heterogeneity analysis of 3D-ECTs

Videos of spontaneously contracting 3D-ECTs were recorded with a Nikon Ti Eclipse phase contrast microscope fitted with an Andor Luca S camera. The contraction videos were converted into TIFF image files using NIS Elements and analyzed with optical flow MATLAB software (3). Macroblocks were assigned to the pixels in the image files to track the motion between frames. This motion was calculated regionally on days 20 and 41 (n = 6 encapsulations for each geometry; analysis was performed on 4 tissues of each geometry per encapsulation and results were averaged). Regions of interest (ROIs) of the microisland and square geometries were analyzed as quadrants, while the rectangular geometry had two ROIs along the longitudinal axis. The values from each ROI for each tissue were averaged to calculate whole-tissue averages. Individual value plots of average contraction velocity, average relaxation velocity, frequency, and time interval between contraction and relaxation were generated. Each data point represents the averaged ROI values for one whole tissue.

The expanded TIFF image files obtained from the contraction videos were used for directionality analysis. The motion between frames was analyzed using the open-source MATLAB code (3), and a directional movie was generated. The center of beating was determined, and the software produced a motion vector field around this point. The maximum contraction and relaxation motion frames were determined from the vector fields, and these individual frames were analyzed with an ImageJ Directionality plug in. A histogram for the angles of each motion vector from -90° to 90° was generated, and the goodness of fit values for these histograms were compared, where a goodness of 0 corresponds to no uniform directionality and a goodness of 1 corresponds to a single directionality.

ImageJ was used to quantify spatial heterogeneity. Phase contrast image frames were extracted from the contraction analysis videos on days 20 and 40. The region of interest tool was used to

outline and quantify the total tissue area. In conjunction with the contraction analysis video, a region of heterogeneity was selected where no tissue contraction was occurring and visual differences in tissue appearance were clear and obvious. To calculate the heterogenous fraction, total heterogenous area was divided by total tissue area.

# Reverse Transcription Quantitative PCR (RT-qPCR)

Two-step RT-qPCR was performed on tissue samples (n=3 tissues of each geometry from independent differentiations) from days 10, 20, and 40. First, total RNA was isolated using a NucleoSpin RNA isolation kit (Machery-Nagel) and RNA yield was quantified using a Nanodrop (Thermo Fisher Scientific). cDNA was synthesized using a SuperScript™ IV First-Strand Synthesis System (Thermo Fisher Scientific).

RT-qPCR was performed using either TaqMan<sup>TM</sup> Fast Advanced Master Mix or Power SYBR<sup>TM</sup> Green PCR Master Mix (Thermo Fisher Scientific) based on previously design primers (4, 5) or new KiCqStart® SYBR® Green Primers (Sigma Aldrich) (Supplementary Table 1) using a QuantStudio<sup>TM</sup> 3. Each Taqman reaction was ran in duplex with GAPDH and contained 5ng cDNA, 200 nM forward and reverse primer (GAPDH and Gene of interest), and 100nM probe (HEX and FAM), and was run at an annealing temperature of 55°C. Each SYBR Green reaction contained 5ng cDNA and 500 nM forward and reverse primers, and was run at an annealing temperature of 58°C. All gene expression levels were normalized using GAPDH and quantified using the 2(-ΔΔCt) method. Primers are listed in Supplementary Table 1.

#### TEM Imaging

day 140 3D-ECTs of each geometry (n=3 tissues of each geometry from 3 independent differentiations) were fixed in 3% glutaraldehyde (Electron Microscopy Science) and shipped at room temperature to the Pathology Electron Microscopy Core facility at the Icahn School of Medicine at Mount Sinai, NY. 3D-ECTs were sectioned (60 nm ultrathin sections), stained with uranyl acetate-lead citrate solution, and imaged using a transmission electron microscope (H-7650, Hitachi High Technologies).

#### Optical Mapping

To assess the electrophysiological properties of 3D-ECTs, optical mapping was performed by using a high-speed camera (Andor iXon+ 860 EMCCD) mounted on a fluorescent camera (Ti Eclipse Nikon) using our previously established optical mapping system (6). Recordings were used to calculate calcium transient duration, external pacing response, and conduction velocity. Day 35 3D-ECTs were incubated in RPMI B27 media containing calcium-sensitive dye Rhod-2 (5 μM, Invitrogen) and blebbistatin (10 μM, VWR) for 2 hours at 37 °C followed by rinsing with Tyrode's Solution (1.8 mM CaCl2, 5 mM glucose, 5 mM HEPES, 1.0 mM MgCl2, 5.4 mM KCl, and blebbistatin 10 μM) before experimentation. Dyed 3D-ECTs were placed in the optical mapping chamber and perfused with warm Tyrode's Solution. Videos were recorded with and without external electrical pacing from 1 Hz to 4 Hz at 20 V. Video recordings were taken in multiple tissue regions per sample and analyzed using a custom MATLAB script in which the change in fluorescence was used to calculate the calcium transient duration (CTD) at 50 and 80 percent repolarization and conduction velocity.

#### **Statistics**

All statistics were performed using Minitab 19. All numerical data is presented as the mean  $\pm$  the standard deviation unless otherwise stated. Data comparing the geometries at a single time point was subjected to General Linear Model analysis while data comparing geometries at multiple timepoints was subjected to Mixed Model Effects analysis to evaluate significant differences with a p < 0.05.

#### References

- 1. DeLong SA, Moon JJ, West JL. Covalently immobilized gradients of bFGF on hydrogel scaffolds for directed cell migration. Biomaterials. 2005;26(16):3227-34.
- 2. Plotkin M, Vaibavi SR, Rufaihah AJ, et al. The effect of matrix stiffness of injectable hydrogels on the preservation of cardiac function after a heart attack. Biomaterials. 2014;35(5):1429-38.
- 3. Huebsch N, Loskill P, Mandegar MA, et al. Automated Video-Based Analysis of Contractility and Calcium Flux in Human-Induced Pluripotent Stem Cell-Derived Cardiomyocytes Cultured over Different Spatial Scales. Tissue Eng Part C-Me. 2015;21(5):467-79.
- 4. Kerscher P, Kaczmarek JA, Head SE, et al. Direct Production of Human Cardiac Tissues by Pluripotent Stem Cell Encapsulation in Gelatin Methacryloyl. ACS Biomaterials Science & Engineering. 2016;3(8):1499-509.
- 5. Kerscher P, Turnbull IC, Hodge AJ, et al. Direct hydrogel encapsulation of pluripotent stem cells enables ontomimetic differentiation and growth of engineered human heart tissues. Biomaterials. 2016;83:383-95.
- 6. Hodge AJ, Zhong J, Lipke EA. Enhanced stem cell-derived cardiomyocyte differentiation in suspension culture by delivery of nitric oxide using S-nitrosocysteine. Biotechnol Bioeng. 2016;113(4):882-94.